Editors' Suggestion

$Pb_9Cu(PO_4)_6(OH)_2$: Phonon bands, localized flat-band magnetism, models, and chemical analysis

Yi Jiang,[1,*] Scott B. Lee,[2,*] Jonah Herzog-Arbeitman,[3,*] Jiabin Yu,[3,*] Xiaolong Feng,[4,*] Haoyu Hu,[1,*] Dumitru Călugăru,[3,*] Parker S. Brodale,[5,*] Eoghan L. Gormley,[5,*] Maia G. Vergniory,[1,4] Claudia Felser,[4] S. Blanco-Canosa,[1,6] Christopher H. Hendon,[5] Leslie M. Schoop,[2,*] and B. Andrei Bernevig[1,3,6,*]

[1]*Donostia International Physics Center (DIPC), P. Manuel de Lardizabal 4, 20018 Donostia-San Sebastian, Spain*
[2]*Department of Chemistry, Princeton University, Princeton, New Jersey 08544, USA*
[3]*Department of Physics, Princeton University, Princeton, New Jersey 08544, USA*
[4]*Max Planck Institute for Chemical Physics of Solids, 01187 Dresden, Germany*
[5]*Department of Chemistry and Biochemistry, University of Oregon, Eugene, Oregon 97403, USA*
[6]*IKERBASQUE, Basque Foundation for Science, 48013 Bilbao, Spain*

(Received 22 August 2023; revised 28 October 2023; accepted 31 October 2023; published 8 December 2023)

In a series of recent reports, doped lead apatite (LK-99) has been proposed as a candidate ambient temperature and pressure superconductor. However, from both an experimental and theoretical perspective, these claims are largely unsubstantiated. To this end, our synthesis and subsequent analysis of an LK-99 sample reveals a multiphase material that does not exhibit high-temperature superconductivity. We study the structure of this phase with single-crystal x-ray diffraction (SXRD) and find a structure consistent with doped $Pb_{10}(PO_4)_6(OH)_2$. However, the material is transparent which rules out a superconducting nature. From *ab initio* defect formation energy calculations, we find that the material likely hosts OH^- anions, rather than divalent O^{2-} anions, within the hexagonal channels and that Cu substitution is highly thermodynamically disfavored. Phonon spectra on the equilibrium structures reveal numerous unstable phonon modes. Together, these calculations suggest it is doubtful that Cu enters the structure in meaningful concentrations, despite initial attempts to model LK-99 in this way. However, for the sake of completeness, we perform *ab initio* calculations of the topology, quantum geometry, and Wannier function localization in the Cu-dominated flat bands of four separate doped structures. In all cases, we find they are atomically localized by irreps, Wilson loops, and the Fubini-Study metric. It is unlikely that such bands can support strong superfluidity, and instead are susceptible to ferromagnetism (or out-of-plane antiferromagnetism) at low temperatures, which we find in *ab initio* studies. In sum, $Pb_9Cu(PO_4)_6(OH)_2$ could more likely be a magnet, rather than an ambient temperature and pressure superconductor.

DOI: 10.1103/PhysRevB.108.235127

I. INTRODUCTION

A wave of scientific and social interest has followed a recent claim that LK-99 [1,2], with the proposed composition of $Pb_{10-x}Cu_x(PO_4)_6O$, exhibits ambient temperature and pressure superconductivity [3–21]. Although the data presented in the original reports is insufficient to support such a remarkable claim, a large body of immediate work has followed. Experimentally, it is unclear what the structure and composition of the material really are; most likely it is a multiphase sample. Experiments have suggested diamagnetic behavior, and levitation experiments have discussed that it may arise from either diamagnetism or small ferromagnetic impurities [8]. As the sample is likely to contain multiple phases, it is possible that two different compounds contribute to each property, i.e., one part is diamagnetic, and the other metallic. Thus clarification of the composition of the material is necessary *before* trusting the models based on postulated structures. Assuming some of the numerous possible compositions, a number of *ab initio* band structures have been produced. Claims of flat bands—and their positive influence on superconductivity—have been made.

However, given the stakes, computation, and prediction of physical properties requires an elevated level of accuracy. While flat bands provide a theoretical platform for high-temperature superconductivity, nontrivial quantum geometry is compulsory for superfluidity, i.e., the Meissner effect [22–32]. This is because the mass of the condensing Cooper pair is inversely proportional to the minimal Fubini-Study metric [33,34], a rigorous measure of quantum geometry. A variety of nonzero lower bounds on the minimal Fubini-Study metric exist for nonatomic bands [22,35–38]. However, flat bands are in fact detrimental to superfluidity if they are atomically localized, i.e., if their narrow dispersion comes from Wannier localization as opposed to destructive interference [39–41]. The inescapability of this conclusion is seen in the limiting case of a tight-binding model with all hoppings vanishing. The perfectly flat band that results cannot support transport of any kind, much less superconductivity, even in the presence of attractive Hubbard interactions. The key physics of flat band superconductivity thus lies in

*These authors contributed equally to this work.

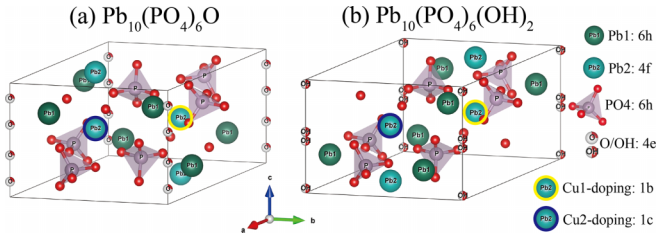

FIG. 1. The crystal structure for (a) $Pb_{10}(PO_4)_6O$ [45] and (b) $Pb_{10}(PO_4)_6(OH)_2$ [5]. The Wyckoff positions of atoms in space group 176 $P6_3/m$ are labeled, with their coordinates given in Table I. The O atoms surrounding P atoms that form PO_4 are at $6h$ or generic positions and are not labeled for simplicity. We also mark two possible Cu doping positions on Pb_2 with yellow and blue circles, which are $1b$ and $1c$ Wyckoff positions in space group 143 $P3$ and will be called Cu1- and Cu2-doping, respectively. The H atoms are not shown in (b) for simplicity, which are close to the trigonal O atoms at $4e$ Wyckoff position.

deviations from this limit, measured by quantum geometry [42]. Furthermore, if Coulomb repulsion overwhelms the would-be attractive interaction, flat band ferromagnetism, rather than superconductivity, would be favored [43,44]. Thus a comprehensive understanding of the active bands at the Fermi level is required for predictions of the many-body state.

Due to new advances in understanding and classification of band structures [46,47], we can analyze their symmetry, localization, and topology with extreme accuracy that only depends on the accuracy of the DFT calculation. In this work, we study two lead apatites (see Fig. 1) available in materials databases, $Pb_{10}(PO_4)_6O$ [45] and $Pb_{10}(PO_4)_6(OH)_2$ [5]—which we emphasize may not be the ultimate material structure. Making assumptions about the location of the fractionally occupied O anion and the Cu dopant, we obtain several microscopic models for the electron and phonon bands in this system. Our results can be summarized as follows.

Firstly in the $Pb_{10}(PO_4)_6O$ initial structure [Fig. 1(a)], we consider Cu replacing Pb at two possible positions, either the 1b or 1c Wyckoff positions, referred to as the Cu1- and Cu2-dopings, respectively. Both possibilities result in a set of two bands at the Fermi level dominated by Cu (see Sec. III A). They are narrow with an ∼100-meV bandwidth, and form an elementary band representation [46] of the Cu d orbitals. We construct four-band, short-ranged, symmetric tight-binding (TB) models for both Cu1 and Cu2 dopings, which demonstrate that the weak dispersion of the Cu orbitals arises primarily from hybridization with nearby O bands. Based on the TB model, we compute the Fubini-Study metric and non-Abelian Wilson loops, which show strong localization, although the Cu2 structure does have a significantly reduced gap to the O bands below. Secondly we consider the $Pb_{10}(PO_4)_6(OH)_2$ structure [Fig. 1(b)]. For both locations of the Cu dopant, we again find a set of Cu bands in an elementary band representation with the ∼100-meV bandwidth. However, the gap to the nearby O bands is much larger, and we provide a two-band model built entirely from Cu Wannier functions. Again, the Fubini-Study metric indicates atomic localization. See Secs. III and IV for more details.

In all cases, the two bands at the Fermi level lack strong quantum geometry. Due to their flat, localized nature, ferromagnetism seems to be the preferred configuration of these states in *ab initio* studies (see Sec. III A). The absence of extended states in these bands does not support a theory of high-temperature superconductivity based on the flat bands we obtain in these structures. However, preliminary calculations of the phonon spectrum show that more careful relaxation of the doped compound is required to fully stabilize their structures, which may result in changes to the band geometry. A phonon-driven mechanism for superconductivity must also compete with the strong Hubbard repulsive interaction, which we also construct using *ab initio* Hubbard-Kanamori parameters. Our Supplementary section [48], including Refs. [1,2,5,9,45,46,49–63], contains more supporting information.

TABLE I. The atomic positions in $Pb_{10}(PO_4)_6O$[45] and $Pb_{10}(PO_4)_6(OH)_2$[5]. The lattice constants for $Pb_{10}(PO_4)_6O$ are $a = 9.865$, $c = 7.431$ Å, and for $Pb_{10}(PO_4)_6(OH)_2$ are $a = 9.866$, $c = 7.426$ Å. The Wyckoff positions in SG 176 have the following coordinates: $4f = (\frac{1}{3}, \frac{2}{3}, z)$, $(\frac{2}{3}, \frac{1}{3}, z + 1/2)$, $(\frac{2}{3}, \frac{1}{3}, -z)$, $(\frac{1}{3}, \frac{2}{3}, -z + 1/2)$, $4e = (0, 0, \pm z)$, $(0, 0, \pm z + \frac{1}{2})$, and $6h = (x, y, \frac{1}{4})$, $(-y, x - y, \frac{1}{4})$, $(-x + y, -x, \frac{1}{4})$, $(-x, -y, \frac{3}{4})$, $(y, -x + y, \frac{3}{4})$, $(x - y, x, \frac{3}{4})$. For both compounds, the Pb_2 atoms at $4f$ approximately lie on the honeycomb lattices on $z = 0, \frac{1}{2}$ planes. The 'tri' in the table stands for trigonal lattice. The tri-O and tri-OH in the two compounds have fractional occupancies, i.e., 1/4 for tri-O and 1/2 for tri-$(OH)_2$.

Compound	Atom	Wyckoff position
$Pb_{10}(PO_4)_6O$	Pb_1	$6h$
	Pb_2	$4f$, $z = 0.004$
	P	$6h$
	tri-O	$4e$, $z = 0.134$, 1/4-occu
$Pb_{10}(PO_4)_6(OH)_2$	Pb_1	$6h$
	Pb_2	$4f$, $z = 0.994$
	P	$6h$
	tri-$(OH)_2$	$4e$, $z = 0.040$, 1/2-occu

II. CHEMICAL STRUCTURE

Pb-apatite is structurally related to the parent compound, Ca-apatite, and much can be learned through their comparison. This crystal type features 1-dimensional channels filled with requisite charge-balancing anions. For example, the calcium-oxo analog has been shown to only exist as $Ca_{10}(PO_4)_6O$ at temperatures exceeding 1000 °C [64] below of which it rapidly includes water into the lattice, forming the neutral hydrate $Ca_{10}(PO_4)_6(OH)_2$. While the Pb-based system may have different dehydration temperatures to interconvert between $Pb_{10}(PO_4)_6O$ [45] and $Pb_{10}(PO_4)_6(OH)_2$ [5] (see Fig. 1), historical data would indicate that the hydrated material is thermodynamically preferred. To this end, we performed a number of DFT calculations to assess the formation enthalpy of the hydroxy and oxo Pb apatites considered here. Our calculations reveal that the inclusion of H_2O, forming $Pb_{10}(PO_4)_6(OH)_2$, is exothermic with its inclusion favored by 38.5 kcal/mol. These data suggest while $Pb_{10}(PO_4)_6O$ may be

a metastable form, direct syntheses of that material will tend to form the hydrate if sufficient protons are available. And even if $Pb_{10}(PO_4)_6O$ is formed it will interconvert to the hydrate upon exposure to air.

Structurally, the oxo and hydroxy apatites are better distinguished by their lattice parameters, and less so by direct crystallographic measurements. Ca-apatite exhibits a dramatic lattice contraction in both the a and c parameters [65], proportional to the extent of hydration, i.e., the conversion from O^{2-} to OH^- contracts the lattice [66]. Such contraction has been attributed to Cu inclusion within the $Pb_{10}(PO_4)_6O$ lattice [2,7], but a similar effect is predicted through simple hydration.

While theoretical studies thus far have focused on the pure $Pb_{10-x}Cu_x(PO_4)_6O$ or $Pb_{10-x}Cu_x(PO_4)_6(OH)_2$ phase, the reported synthesis methods cannot result in single phase samples of either of them. In the final step of the reaction, Lanarkite ($Pb_2(SO_4)O$) is mixed in a 1:1 molar ratio with Cu_3P, but this 2:1 Pb/P ratio is stoichiometrically inconsistent with the desired product. Even loosening the ratio of the reactants would create a significant amount of Cu impurities: the final product has 6 P, so there will be 18 Cu per formula unit of $Pb_9Cu_1(PO_4)_6O$ or $Pb_9Cu_1(PO_4)_6(OH)_2$. The powder x-ray diffraction (PXRD) pattern presented in the original reports [1,2] suggests that the majority of the sample exists in a structure related to $Pb_{10}(PO_4)_6(OH)_2$, but also features many crystalline impurities. Due to the severe off-stoichiometry of the reaction, additional amorphous phases are also to be expected. Only a few Rietveld analyses have thus far been performed [12], and it is difficult to separate the structural effects of Cu inclusion versus hydration without high-quality single crystal data. To this end, is unclear if *any* Cu atoms were actually incorporated into the structure.

To address this, we are able to compute the formation enthalpies of Cu substitutions at Pb lattice sites. Following the standard procedure [52], the Cu defects were computed using a $2 \times 2 \times 2$ super cell containing 1831 electrons for the neutral substitution. Computations were referenced to bulk Cu/Pb (rich potentials) and CuO/PbO (poor potentials) and the formation enthalpy was computed using a $2 \times 2 \times 2$ k-mesh, with the FNV correctional scheme employed for charged defects and averaged diagonalized dielectric tensors [67,68], and Hubbard model ($U = 4.0$ eV for Cu). The formation enthalpies for the defects are depicted in Fig. 2. Notably, the experimentally observed Cu^{2+} (i.e., charge-neutral) substitution is predicted to form in p-type conditions, at minimum occurring with a 1.2 eV penalty depending on the reference potentials and amounting to many orders of magnitude sub-stoichiometric Cu concentration, essentially forbidding its ordered inclusion within the material. However, the charge transition from the inclusion of Cu^{2+} to Cu^{1+} occurs very near the Fermi level for the undoped Pb-apatite material, and Cu^{1+} inclusions become more favored in n-type conditions. The experimental absence of appreciable Cu^{1+} suggests that if Cu^{2+} is incorporating, it is being aided by other correlated defects not considered here. Additionally, other mechanisms of Cu inclusion are possible (e.g., interstitial formation, as observed in Pb^{2+}-containing lead halide perovskites [69]). Pb-apatite may host other dopants, e.g., S, which is also present during the reaction [70]. These may be studied in future work.

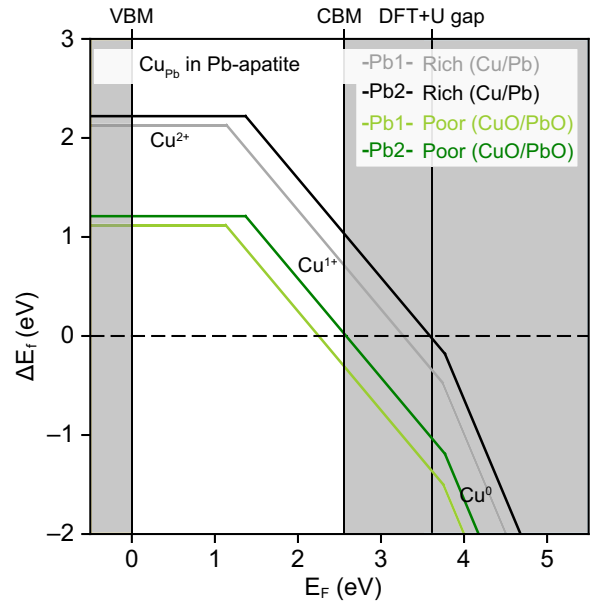

FIG. 2. The defect formation enthalpies for Cu substitution in Pb lattice sites at both rich and poor potentials show that Cu_{Pb} is unfavorably incorporated into either Pb site within the apatite lattice.

To address whether Cu and OH^- are included, and to generally deduce the structure, we performed a modified synthesis of the putative LK-99 compound described in Refs. [1,2]. Relative sample purity of all intermediate reagents was confirmed via powder x-ray diffraction using a STOE Stadi P powder x-ray diffractometer equipped with a Mo Kα ($\lambda = 0.71073$ Å) sealed-tube x-ray source and graphite monochromator at room temperature in either Debye-Scherrer or transmission geometry (see Sec. III in Ref. [48]). For synthesis of $Pb_2(SO_4)O$, minor impurity peaks in the pattern are consistent with small amounts of unreacted $Pb(SO_4)$. In the final step, Cu_3P and $Pb_2(SO_4)O$ mixed in a 1:1 molar ratio were ground into a fine powder in mortar and pestle. The powders were loaded into an alumina crucible, placed in a quartz tube, and sealed under dynamic vacuum without any argon back-filling. The tube was then loaded in a furnace and heated to 950 °C over 4 hours, kept at this temperature for 6 hours, and then shut off to cool quickly. Upon pulling the sample out of the furnace we observed that our sample, due to its loading in an alumina crucible, did not attack our quartz tube in contrast to Refs. [1,2]. This suggests the possibility of further chemical reactions in the protocol of Refs. [1,2]. The resulting product inside the crucible contained mostly white and orange colored powder in addition to metallic gray lumps as seen in Fig. 16 in Sec. III in Ref. [48]. A PXRD pattern of this sample can be seen in Fig. 15 in Sec. III in Ref. [48], showing that our sample has more impurity phases than the original LK-99 sample, but that the characteristic peaks are present and thus it seems possible to isolate the main phase reported in the original sample from our sample as well. Energy-dispersive x-ray spectroscopy (EDS) was also utilized to examine these impurity phases. In Fig. 17 in Sec. III in Ref. [48], we show that the transparent-orange phase likely gets its color from pockets of metallic Cu. Likewise, in Fig. 18 in Sec. III in

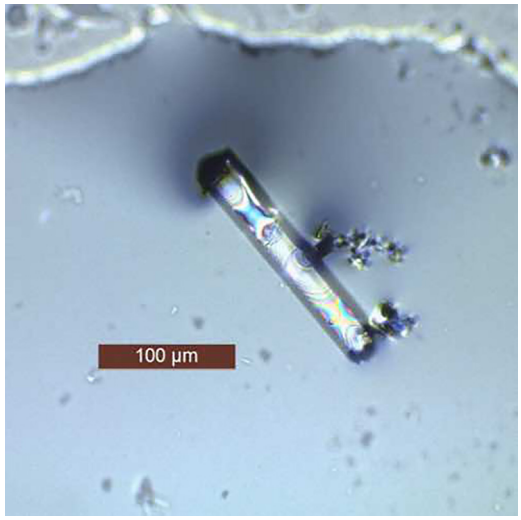

FIG. 3. A single crystal similar in transparency, shape, and size to what we picked for SXRD.

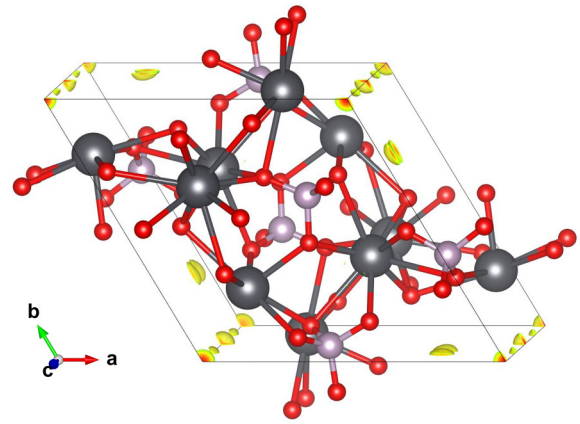

FIG. 4. Residual electron density located at the 2a and 2b positions along the c axis. Positive isosurfaces are drawn at 7e $Å^{-3}$.

Ref. [48], we observe islands of Cu_2S embedded in a matrix of the transparent-white phase. As noted previously [71,72], these Cu_2S islands are likely the cause of the tenfold drop in resistivity observed at 104.8 °C in the original preprint.

Under magnification, the white powder was observed to be transparent single crystals with a clear hexagonal rod habit (Fig. 3). Knowing that $Pb_{10}(PO_4)_6O$ was reported to crystallize in a hexagonal space group, a transparent single crystal of dimensions (0.55 × 0.092 × 0.176 mm) was picked for single crystal x-ray diffraction (SXRD) analysis using an APEX2 CCD diffractometer equipped with a Mo K_α ($\lambda = 0.71073$ Å) sealed-tube x-ray source and graphite monochromator at room temperature. Initial unit cell refinement obtained a unit cell in a hexagonal setting with lattice parameters $a = 9.8508(1)$ Å and $c = 7.4395(2)$ Å, agreeing with other previously reported structures for lead apatite [5,45]. Indexation and integration proceeded smoothly for a full hemisphere collection out to a resolution of 0.5 Å. Run list generation and frame data processing were done in APEX 2 [73]. An analytical absorption correction was used to scale the data before importing the peak list into JANA2020 [74].

The initial structure solution was obtained in space group $P6_3/m$, consistent with observed systematic absences (Fig. 19 in Sec. III in Ref. [48]), from the charge-flipping algorithm as implemented in SUPERFLIP [75]. An initial refinement, done on F^2, was needed to obtain a valid initial structure with six distinct sites (2 Pb, 1 P, and 3 O). Notably, during this initial refinement Oxygen atoms along the c axis were removed. Running a Fourier transform of residual electron density, visualized with the VESTA software package [76], reveals 2 unique crystallographic pockets of significant electron density around points [0 0 0] (Wyckoff position 2*b*) and [0 0 1/4] (2*a*) in $P6_3/m$, shown in Fig. 4, suggestive of a $Pb_{10}(PO_4)_6(OH)_2$ structural solution. After Oxygen atoms were added to these points, freely refining their occupancies results in a site occupancy factor of the 2*b* oxygen centered at [0 0 0] of 1.163, an unphysical value for an OH^- molecular unit. Clearly, an atom with more electron density is needed. Replacing the oxygen instead with sulfur, a chemically similar element that is also present in the reaction, seems like a likely candidate, although further elemental analysis methods will be needed to distinguish between an SH^-, PH_2^-, or other possible dopants at this site.

Freely refining occupancies for both an O at [0 0 1/4] and S located at [0 0 0] results in site occupancy factors of 0.54 and 0.56, respectively. The freely refined occupancies having a summation very close to 1 seems suggestive that this could be a physically real interpretation of the structural solution. After refining the isotropic parameters anisotropically, a final refinement converges with a goodness of fit (GoF) parameter of 1.22 and R value of 3.94 compared to all reflections. Here, our site occupancies for O (1.08) and S (1.12) sum to above 1. If we decide to restrict the occupancies of the 2*b* S and 2*a* O to sum to a site occupancy factor of 1, we end refinement with a final composition $Pb_{10}(PO_4)_6(OH)_{0.94}(SH)_{1.06}$. This refinement has nominally the same refinement statistics [GoF(all) = 1.22, R(all) = 3.95].

We also investigated two ways of possible Cu doping within our refinement: one in which the Cu atom substitutes on the Pb lattice site, and another which the Cu atom is inserted along the chain. Attempts to dope both Pb sites with Cu results in a refined composition of $Pb_{9.55}Cu_{0.45}(PO_4)_6(OH)_{0.94}(SH)_{1.06}$ with similar statistics [GoF(all) = 1.21, R(all) = 3.93]. We found the Cu has to be added in as a split site after the Pb position has been refined completely. The last two steps of occupancy and anisotropic parameter refinement had to be done by restraining the Pb/Cu split site position with automatic refining keys switched off.

The compositional refinement of this structure certainly warrants skepticism. Unfortunately for us, this system has complications for EDS, namely, the Pb $L_{\alpha 1}$ edge lies at the same energy as the S $K_{\alpha 1}$ edge. This, along with neutron diffraction being needed to confirm H incorporation means future studies are needed. However, in an attempt to confirm the Cu incorporation suggested by our refinements, we carbon coated a small transparent needle and ran EDS on a Quanta environmental scanning electron microscope. Using the elemental mapping technique, we were surprised to find that we were able to detect Cu, and it is homogeneously distributed

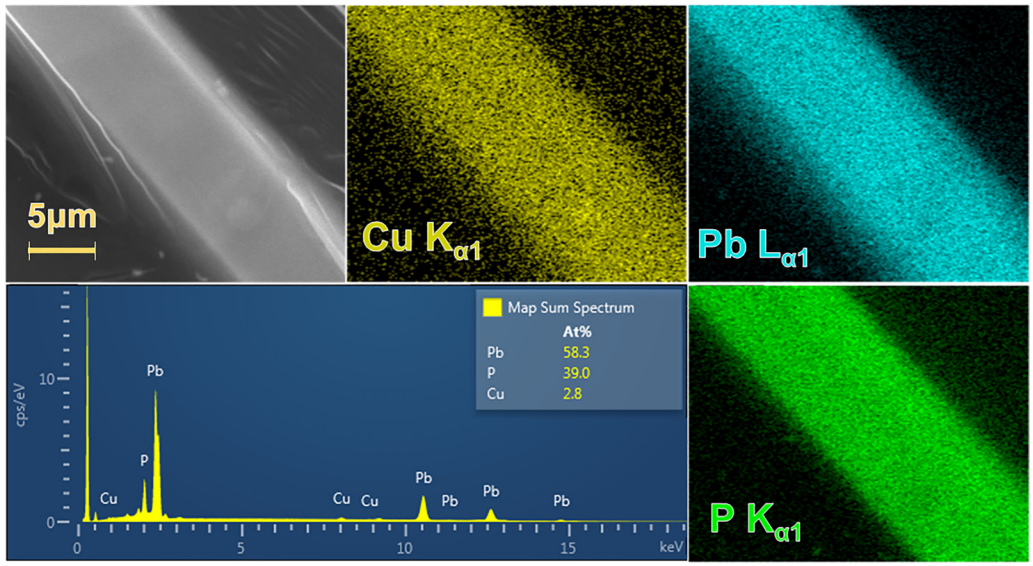

FIG. 5. Energy dispersive x-ray spectroscopy map of a translucent crystal coated in carbon.

within the crystal. Furthermore, in Fig. 5, the Pb:Cu ratio we detected over a roughly 15-minute period was 58.3:2.8, which roughly translates to a ratio of 9.55:0.46, an indicator that the Cu incorporation in our refined composition of $Pb_{9.55}Cu_{0.45}(PO_4)_6(OH)_{0.94}(SH)_{1.06}$ could be correct. However, we would like to acknowledge the fact that 2.8 atomic percent is extremely low for EDS characterization and future studies utilizing synchrotron radiation are needed to confirm incorporation. In addition, as there is a lot of Cu in the reaction it cannot be ruled out that Cu is at the surface of the crystal.

We can also obtain a reasonable refinement to the data if we place Cu into the channel with composition $Pb_{10}(PO_4)_6(OH)_{1.11}$ $Cu_{0.49}$ (GoF = 1.22, R = 3.93). Still, as the crystals are transparent, charge balance needs to be maintained and thus this last solution is not chemically reasonable. Full collection, integration, and refinement statistics can be found in Sec. III in Ref. [48]. We would like to stress here again that the transparent nature of the crystal should rule out superconductivity as a property, it rather indicates a wide band gap.

Next, we compare simulated powder patterns of our structural solution, the ICSD reported structures, and the relaxed DFT structures of Cu-doped variants with the published PXRD pattern from [1,2]. To do this, structural position files were loaded into VESTA, and patterns simulated for using a Cu K_α ($\lambda = 1.5406$ Å) wavelength. Simulated patterns were then overlaid atop the experimental pattern, extracted using an in-house Mathematica code. For ease of visualization, we adjust the simulated patterns via a zero point shift to match the peaks expected around 18° in the experimental data. This zero-point correction is not uncommon for Rietveld refinements and is needed if the diffractometer used in the experimental pattern is misaligned. Most zero-point corrections were minimal, i.e., 0.2°. We find a good agreement (see Sec. III in Ref. [48]) of our SXRD solution with the reported data. Other structures fit the data less well and a discussion is given in the SI. This analysis is preliminary as the cropped data from the original preprint are not of high enough quality to perform a Rietveld analysis. It does however show that our structure obtained from SRXD, measured in a *transparent* crystal, agrees with the powder pattern published in the original LK-99 paper. Further analysis of our samples will follow.

Due to the numerous uncertainties regarding the ultimate structural composition of the LK-99 material, we will investigate a variety of scenarios using *ab initio* density functional theory. In our *ab initio* studies, we still focus on structures on which Cu substitutes for Pb, as we come to different conclusions as previous theoretical works assuming the same substitutions.

III. AB INITIO RESULTS

We consider two different experimental structures of lead apatite for *ab initio* calculations in this work, i.e., $Pb_{10}(PO_4)_6O$ [45,77] and $Pb_{10}(PO_4)_6(OH)_2$ [5,78], both have space group (SG) 176 $P6_3/m$ symmetry. Their crystal structures are shown in Fig. 1. The O atoms at 4*e* Wyckoff position in $Pb_{10}(PO_4)_6O$ have 1/4 occupancy, while the hydroxyl groups at 4*e* in $Pb_{10}(PO_4)_6(OH)_2$ have 1/2 occupancy. The atomic positions are summarized in Table I. We remark that lead apatite has many experimentally reported structures, with the position of trigonal-O or $(OH)_2$ being slightly different. For example, the structures in Refs. [79–82] has trigonal-$(OH)_2$ located at Wyckoff position $2a = (0, 0, \frac{1}{4}), (0, 0, \frac{3}{4})$ without fractional occupancy. The LK-99 [1,2] $Pb_{10-x}Cu_xPO_4)_6O$ ($0.9 < x < 1.1$) is hypothesized to be synthesized by doping Pb atoms with Cu at 4*f* Wyckoff positions.

A. Electronic structure

In this section, we discuss the electronic structures for $Pb_{10}(PO_4)_6O$ and $Pb_{10}(PO_4)_6(OH)_2$ in both undoped and Cu-doped phases.

We first consider the undoped phase. As reported in literature [5,45], the trigonal-O in $Pb_{10}(PO_4)_6O$ has 1/4 occupancy, while the trigonal-$(OH)_2$ in $Pb_{10}(PO_4)_6(OH)_2$ has 1/2 occupancy. Such fractional occupancy is difficult to treat in DFT.

For simplicity, we fix their positions to remove the fractional occupancy, i.e., fix O at (0,0,0.634), and fix O in OH_2 at (0,0,0.04),(0,0,0.54) and H at $(0, 0, -0.10)$, $(0, 0, 0.40)$, the total number of electrons in the unit cell is the same as the fractionally occupied structure. Mind that the positions of H atoms are not given in the original experimental structure [5] we use and are manually added using the O-H bond length in H_2O molecular, i.e., about 1Å, which also agrees with the O-H length reported in another experiment structure [83]. Notice that after fixing the trigonal-O and $(OH)_2$ positions, the original SG 176 $P6_3/m$ symmetry is lowered to SG 143 $P3$ and SG 173 $P6_3$ for two structures, respectively. Remark that fixing trigonal-O at any of the four 4*e* positions are equivalent by assuming periodic boundary condition, as they are related by $\{C_{6z}|00\frac{1}{2}\}$ and $\{M_z|000\}$ in SG 176. For trigonal $(OH)_2$, the scenario is similar. Thus we will focus on the aforementioned positions of trigonal-O and $(OH)_2$ in the following. We remark that fractional occupancy can be treated more rigorously using a supercell approach and the special quasirandom structure (SQS) method [84] to generate atomic configurations. Also, for $Pb_{10}(PO_4)_6(OH)_2$, the $1/2$ occupancy of OH only leads to a small oscillation of atomic position around (0,0,0) and $(0, 0, \frac{1}{2})$ in different unit cells (see Table I). Thus we infer that using a large supercell that simulates the disorder will not change the result quantitatively.

After fixing O or $(OH)_2$ positions to remove the fractional occupancy, we relax all the atoms in the structure and obtain the relaxed lattice constants and atomic positions summarized in Sec. I in Ref. [48]. Remark that if one first relaxes the structure without O or OH and then places them in experimental positions, the result could be unreasonable. This is because, without O or OH, the material is not chemically balanced and could make the insulating system metallic. Thus it cannot give properly relaxed structures.

The symmetry is maintained during the relaxation, i.e., SG 143 for $Pb_{10}(PO_4)_6O$ and SG 173 for $Pb_{10}(PO_4)_6(OH)_2$. The band structures for two relaxed structures are shown in Fig. 6, which host a large band gap of 2.761 and 2.635 eV, respectively. The highest occupied bands are quasiflat and mainly come from the (p_x, p_y) orbitals of the trigonal-O atoms.

We then consider the Cu-doped phases. As hypothesized in Refs. [1,2], the Cu-doped LK-99 $Pb_{10-x}Cu_x(PO_4)_6O$ $(0.9 < x < 1.1)$ has Cu doping the Pb atoms at $4f$ position. By fixing $x = 1$ for simplicity, there exist four possible Cu-doping structures by placing the Cu atom at one of the $4f$ positions. The four $4f$ positions are equivalent in SG 176. However, after fixing $(OH)_2$ in $Pb_{10}(PO_4)_6(OH)_2$, the SG is lowered to SG 173 $P6_3$, which gives two inequivalent Cu doping positions, which we call the one at $(\frac{1}{3}, \frac{2}{3}, z)$ Cu1-doping and $(\frac{2}{3}, \frac{1}{3}, -z)$ Cu2 doping, as marked using yellow and blue circles in Fig. 1. For $Pb_{10}(PO_4)_6O$, after fixing the position of trigonal-O, the SG is lower to 143 $P3$ which makes all four positions inequivalent. For simplicity, we only consider the Cu1 doping and Cu2 doping, as the other two possible dopings have similar band structures as reported in Ref. [14].

We relax the structure of Cu1- and Cu2-doping for $Pb_{10}(PO_4)_6O$ and $Pb_{10}(PO_4)_6(OH)_2$, both having SG 143 $P3$ symmetry, with lattice constants and atomic positions summarized in Sec. I A in Ref. [48]. The four relaxed structures are used to perform DFT calculations. We consider the paramagnetic (PM) phase and ferromagnetic (FM) for each structure, with their band structures shown in Figs. 7 and 8, and the orbital projections given in Sec. I B in Ref. [48].

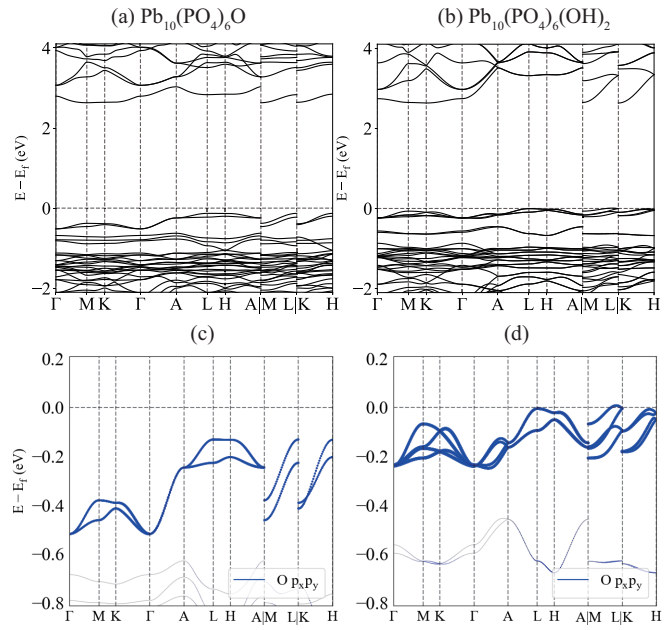

FIG. 6. Electronic band structure for undoped (a) $Pb_{10}(PO_4)_6O$ and (b) $Pb_{10}(PO_4)_6(OH)_2$, and zoom in plots in (c) for $Pb_{10}(PO_4)_6O$ and (d) for $Pb_{10}(PO_4)_6(OH)_2$. The quasiflat bands near E_f are mainly formed by the (p_x, p_y) orbitals of the trigonal-O atoms, which are shown with blue weights.

In the PM phase, for all four structures, there exist two quasiflat bands with $\frac{3}{4}$ filling at the Fermi level E_f, contributed

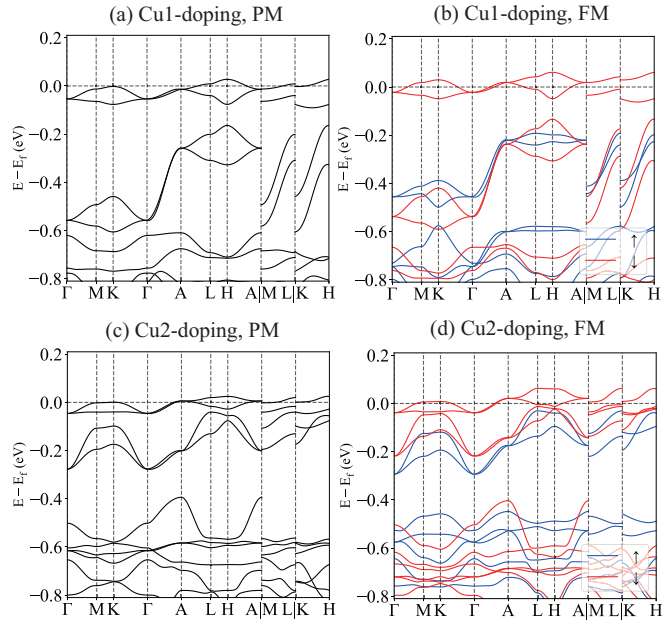

FIG. 7. Electronic band structure for $Pb_9Cu_1(PO_4)_6O$, where (a) is the PM phase and (b) is the FM phase of Cu1 doping. (c) and (d) are similar for Cu2 doping.

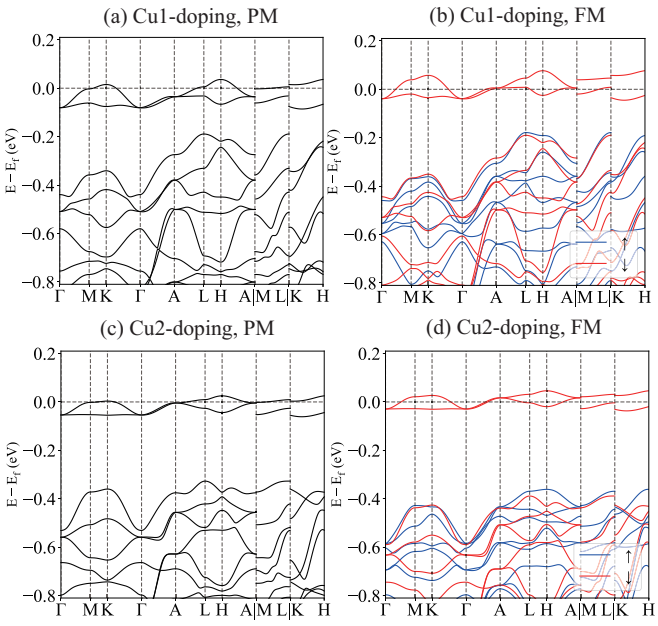

FIG. 8. Electronic band structure for $Pb_9Cu_1(PO_4)_6(OH)_2$, where (a) is the PM phase and (b) is the FM phase of Cu1 doping. (c) and (d) are similar for Cu2 doping.

mainly by the (d_{xz}, d_{yz}) orbitals of Cu (with Cu (d_{xz}, d_{yz}) weight about 50%, $(d_{xy}, d_{x^2-y^2})$ about 20%, and p orbital of O atoms that close to Cu weight about 30%), forming elementary band representation (EBR) ${}^1E^2E@1b$ in SG P3 (notice in the PM phase the time-reversal symmetry exists and enforces ${}^1E$ and ${}^2E$ to be degenerate) for Cu1 doping and ${}^1E^2E@1c$ for Cu2 doping. For two Cu dopings of $Pb_{10}(PO_4)_6O$, there are two bands close the to Cu bands with a small band gap, mainly formed by the bands of (p_x, p_y) of the trigonal-O and form EBR ${}^1E^2E@1a$, as shown in Fig. 7 and orbital projections in Sec. I B in Ref. [48]. Although here these four bands formed by (d_{xz}, d_{yz}) of Cu and (p_x, p_y) of the trigonal-O do not have band inversions and are topologically trivial, we can adjust the hoppings and make them topological, which we show in Sec. IV using minimal tight-binding models. For two Cu dopings of $Pb_{10}(PO_4)_6(OH)_2$, however, the bands below the Cu bands have a larger band gap and weak hybridization with Cu bands.

The FM phases of the four structures all have a lower total energy compared with the PM phase, as shown in Table II, suggesting that the FM phase is energetically more favored than the PM phase. Evidence for soft ferromagnetism, consistent with the well-localized bands and strong Coulomb repulsion we find, has recently appeared in experiments [8]. In the spin-polarized orbital projections shown in Sec. I B in Ref. [48], the quasiflat bands of Cu near E_f have a large spin splitting of about 0.6 eV, while the bands of trigonal-O have negligible spin splitting. The calculated magnetic moment is about 0.6 μ_B for Cu and small moments for O atoms surrounding Cu which sum to about 0.3 μ_B in total, in agreement with the fact that the two flat bands near E_f in the PM phase also have about 30% weight from O. We also calculate the total energy of the A-type antiferromagnetic phase (AFM), i.e., FM inplane and AFM out of the plane, as shown in Table II. The

TABLE II. Comparison between total energy of PM, FM, and A-type AFM phases per unit cell (in eV) calculated in DFT. The total energies in the Cu1-doping phase in $Pb_{10}(PO_4)_6O$ and $Pb_{10}(PO_4)_6(OH)_2$ are used as zero. It can be seen that in all four cases, the FM and AFM phases have very close total energy, which are both lower than the PM phase. In $Pb_{10}(PO_4)_6O$, the Cu1 doping has lower energy while in $Pb_{10}(PO_4)_6)(OH)_2$, the Cu2 phase is lower.

Compound	Phase	PM	FM	AFM
$Pb_{10}(PO_4)_6O$	Cu1 doping	0	−0.129	−0.130
	Cu2 doping	0.195	0.089	0.092
$Pb_{10}(PO_4)_6(OH)_2$	Cu1 doping	0	−0.136	−0.136
	Cu2 doping	−0.177	−0.332	−0.332

FM and AFM phases have almost the same energy per unit cell, both being lower than the PM phase. We leave for future studies to investigate the magnetic ground state.

B. Phonon spectrum

In this section, we perform the phonon calculations to check the stability of proposed structures in the literature, including $Pb_{10}(PO_4)_6O$, $Pb_{10}(PO_4)_6(OH)_2$, $Pb_9Cu_1(PO_4)_6O$ and $Pb_9Cu_1(PO_4)_6(OH)_2$. We find that, in their nominal 111 unit cells (i.e., the original unit cell), *all* structures display imaginary phonon frequencies. We focus our discussion below on $Pb_9Cu_1(PO_4)_6(OH)_2$ since powder x-ray diffraction shows a strong similarity between it and LK-99. Supplemental figures for other structures may be found in Sec. I D [48].

For the undoped structures, both the Pb-O and Pb-$(OH)_2$ present negative/imaginary phonon at low T and high T with $1 \times 1 \times 1$ cell, where the phonon of Pb-$(OH)_2$ is shown in Figs. 9(a) and 9(b). Here, the temperature effect is included via electronic smearing in the harmonic approximation level. As the atomic projection presents, the phonon instability is mainly contributed—as theoretically expected—by the heaviest Pb atoms at both Pb1 and Pb2 sites. As the temperature goes higher, the imaginary phonons harden, especially in the $k_z = 0$ plane where imaginary modes disappear at high T. Since the calculation is performed in $1 \times 1 \times 1$ cell with a short c compared to a, the negative phonon in $k_z = \pi$ plane may be caused by the short cutoff in the c direction. To verify this scenario, we also perform phonon calculation in $1 \times 1 \times 2$ supercell at high T. As shown in Fig. 9(c), the negative branches on the $k_z = \pi$ plane in the $1 \times 1 \times 1$ cell calculation become positive, as the cell is enlarged to include the force constants between atoms with longer distance. We expect that the residual imaginary phonon at the Γ point can be eliminated by performing phonon calculations in a larger supercell after relaxation. We remark that there exist more advanced methods that could give a better description of the temperature effects on phonons compared with the electronic smearing method, including quasiharmonic calculations, stochastic self-consistent harmonic approximation (SSCHA) [85], and temperature-dependent effective potentials (TDEP) [86], which we leave for future studies.

We also observe that the phonon spectrum presents a good separation of frequency based on the mass of elements: the heaviest Pb dominates the lowest frequency and gives the

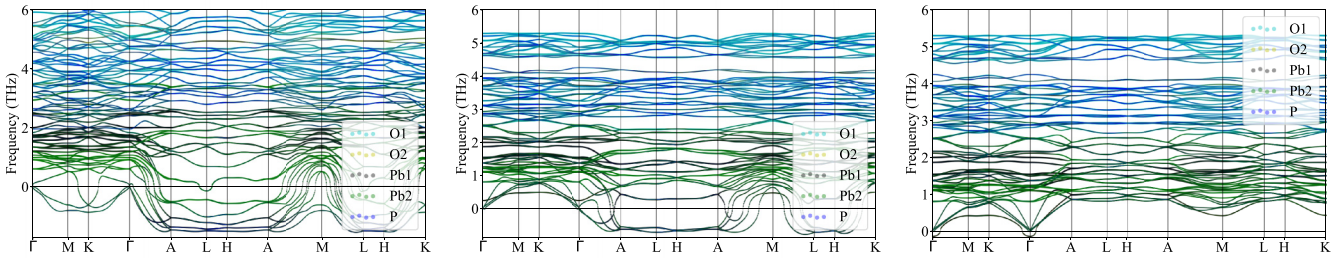

(a) Pb-$(OH)_2$ at low-T. (b) Pb-$(OH)_2$ at high-T. (c) Pb-$(OH)_2$ at high-T in 112 supercell.

FIG. 9. Phonon spectrum for relaxed $Pb_{10}(PO_4)_6(OH)_2$ (without Cu doping) structure at (a) low and (b) high temperature calculated using $1 \times 1 \times 1$ supercell, which shows imaginary, unstable phonons in the $k_3 = \pi$ plane (i.e., $k_z = \frac{\pi}{c}$ plane which contains the *A-L-H-K* lines, where c is the lattice constant in the z direction). (c) Phonon spectrum calculated using a $1 \times 1 \times 2$ supercell at high temperature, which stabilizes the $k_3 = \pi$ modes but softens a single mode at the Γ point. In addition, we observe that the soft phonon modes shown in (a) and (b) are flat modes in the $k_3 = \pi$ plane. A series of flat phonon modes are also presented at the finite frequency in the high-T calculations, such as flat modes around 1 THz in (c).

imaginary modes, H phonons lie at a much higher frequency, which is not shown in the plot, and P and O phonons lie in the middle.

For the Cu-doped structure, previous DFT calculations suggest a (ferro/antiferro)magnetic ground state. Therefore, the phonon calculations are performed in both paramagnetic and ferromagnetic phases as presented in Sec. I D in Ref. [48], with a $1 \times 1 \times 1$ cell. Similar to the undoped case, the doped structures show negative phonon modes, but tend to harden in the FM phase. Both O and the Cu dopant contribute to the imaginary phonon at low T and one should relax the structure with much care for the doping effect to obtain a stable phonon spectrum. We remark that further relaxation in a supercell could be important to stabilize the phonon, especially for disordered systems [87], which we leave for future studies. The difficulty in obtaining a stable structure even for the undoped parent compounds, which exist in nature, underscores an important challenge for first principles studies of the doped compound, whatever its nature.

IV. TIGHT-BINDING MODELS

In this section, we construct short-range tight-binding models for both $Pb_9Cu_1(PO_4)_6O$ and $Pb_9Cu_1(PO_4)_6(OH)_2$ compounds and for both considered positions of the Cu dopant. Such models are a prerequisite for studying the many-body phases that LK-99 is conjectured to realize. We emphasize that the precise chemical composition, purity, and structure of the supposed compound are far from being settled, and initial proposals may need to be re-examined. Nevertheless, we study the *proposed* structures here for completeness. We find, in all cases and in agreement with independent calculations, that Cu forms a high-density flat band at the Fermi level. Based on this finding we ask whether a flat band superconductivity scenario is viable. We perform the calculations of the quantum geometry in these bands and find that they are atomically localized and will likely not favor superconductivity.

In all cases, we find that the two bands straddling the Fermi level are atomic and dominated by the Cu d-orbitals. In the $Pb_9Cu_1(PO_4)_6O$ structure, a four-band model is required due to the close proximity of the O bands, which hybridize with the Cu orbitals particularly in the $k_z = \pi$ plane. For this structure, the dispersion of the Cu bands is predominantly due to hybridization with O. In contrast, $Pb_9Cu_1(PO_4)_6(OH)_2$ shows well-isolated Cu bands at the Fermi level, and a two-band model can be constructed. Section II in Ref. [48] contains a complete discussion of the parameters, symmetry, and quantum geometry of the bands.

A low-energy model of the flat bands can be constructed from the d_{yz}, d_{xz} orbitals of Cu on the 1b/1c positions for Cu1/Cu2 doping, and the p_x, p_y orbitals of O on the 1a position in space group $P3$ for conventions of the lattice). Our DFT calculations show degeneracies at Γ and A (which form double Weyl points [9]) that cannot be protected by C_3 alone since they form an Abelian group. We check that the separate spin sectors possess a spin-less time-reversal symmetry $\mathcal{T}^2 = +1$ which protects a 2D complex irrep ${}^1E\,{}^2E$ arising from the d and p orbitals. The preservation of the spin-less $\mathcal{T}$ in the FM phase comes from the fact that the magnetization is taken into account as the local momentum term $M(\boldsymbol{r})s_z$ (with real scalar $M(\boldsymbol{r})$). The spin-orbital coupling is negligible for the Cu and O atoms.

A. $Pb_9Cu(PO_4)_6O$

In the $Pb_9Cu(PO_4)_6O$ structure, it is necessary to construct a four-band model due to the O-dominated bands that appear closely below (and hybridize with) the Cu-dominated bands at the Fermi level. The model takes the form

$$h_4(\mathbf{k}) = \begin{pmatrix} h_C(\mathbf{k}) & h_{CO}(\mathbf{k}) \\ h_{CO}^\dagger(\mathbf{k}) & h_O(\mathbf{k}) \end{pmatrix} \tag{1}$$

consistent with these symmetries. For Cu1 doping, it is sufficient to include the three nearest-neighbor Cu-O hoppings ($h_{CO}(\mathbf{k})$), six O-O in-plane hoppings for O and Cu, and the two O-O vertical hoppings ($h_O(\mathbf{k})$). In fact, the Cu hoppings are less than 4meV and can be safely dropped, effectively setting $h_C(\mathbf{k}) = 0$. The Cu2 doping structure exhibits a smaller gap between the O and Cu bands and requires the inclusion of the next nearest neighbor hoppings, with full expressions given in Sec. II in Ref. [48]. We find excellent agreement with the DFT spectrum and irreps in Fig. 10 within this approximation.

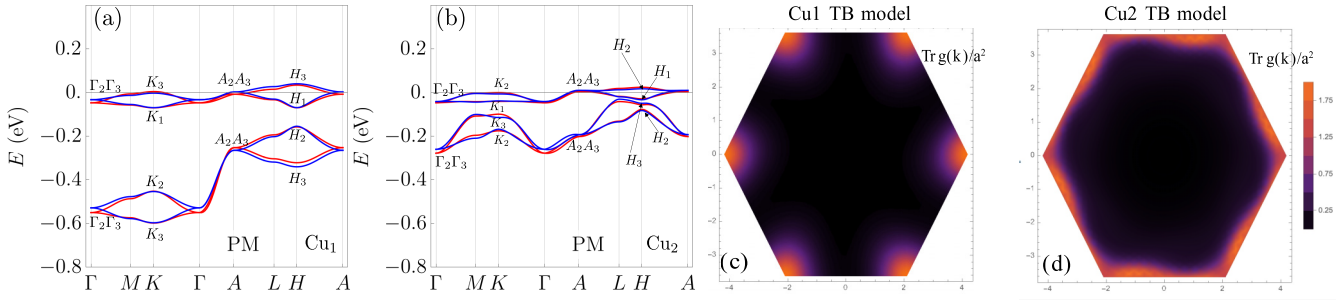

FIG. 10. Comparison of DFT and tight-binding model band structures for $Pb_9Cu(PO_4)_6O$. The relaxed DFT (red) and short-range tight-binding model (blue) are shown for Cu1 doping (a) and for Cu2 doping (b). The 2D quantum metric $g(\mathbf{k})$ is computed on the plane $k_3 = \pi$ for the Cu1 (c) and Cu2 (d) models, showing peaked features where the Cu and O bands have the smallest direct gap.

Our tight-binding model shows that the dispersion of the Cu bands at the Fermi level arises essentially in its entirety from hybridization with O. Nevertheless, symmetry eigenvalues indicate that the bands are topologically trivial: O hybridization does not cause a topological change. To confirm this, we compute the 2D Fubini-Study quantum metric [Figs. 10(c) and 10(d)]

$$g(\mathbf{k}) = \frac{1}{2}\sum_{i=x,y} \mathrm{Tr}\,\partial_i P(\mathbf{k})\partial_i P(\mathbf{k}), \tag{2}$$

where $P(\mathbf{k}) = U(\mathbf{k})U^\dagger(\mathbf{k})$ is the projector onto the eigenvector matrix $U(\mathbf{k})$ of the two Cu bands, and non-Abelian Wilson loop

$$W(k_2, k_3) = U^\dagger(2\pi, k_2, k_3) \prod_{k_1}^{2\pi \leftarrow 0} P(\mathbf{k})\, U(0, k_2, k_3) \tag{3}$$

computed over the set of two bands at the Fermi level. Both show strongly localized states, consistent with their elementary band representation. Furthermore, the basis Wannier functions are localized: the square root of Wannier spread is about $0.20a \approx 0.26c$ for Cu and about $0.33a \approx 0.43c$ for O. As we can see, the Wannier function is more localized for Cu than that for O, explaining the fact why the hopping among Cu is smaller than that among O.

B. $Pb_9Cu(PO_4)_6(OH)_2$

We construct a two-band model $h_2(\mathbf{k})$ for the two bands near the Fermi level in $Pb_9Cu(PO_4)_6(OH)_2$ for both Cu1 doping and Cu2 doping and in both PM and FM phases. The two-band model is constructed with d_{xz} and d_{yz} on Cu (at 1b for Cu1 doping and at 1c for Cu2 doping), and it only contains NN hopping along all three directions in addition to the onsite energy term. The form of the model is the same for both doping and for both PM and FM phases, since they all preserve the spinless TR and C_3 symmetries for the two bands near the Fermi level according to the Wannierization of DFT data. With parameter values determined from the Wannierization of the DFT data, we can see that the model gives very similar bands as the DFT band structure (Fig. 11). (Detailed expression and parameter values of the two-band model can be found in Sec. II B in Ref. [48].)

In particular, for one specific Cu doping, we choose the same parameter values for the NN hoppings for PM and FM phases, since the DFT values in the two phases are very close (difference smaller than 0.1 meV); the only non-negligible difference between PM and FM is just an onsite energy shift, indicating that the effect of FM on the states near Fermi level is just uniformly shifting their energy. The small bandwidth of the bands near the Fermi level comes from the small hopping magnitudes (maximum hopping about 12 meV), which comes from the small spread of the Wannier function of the basis (the square root of the Wannier spread of each orbital is about $0.24a \approx 0.32c$). We can see the Wannier spread of the two-band model is larger than that of the Cu in the four-band model, which is consistent with the larger hopping here compared to the hopping among Cu in the four-band model.

In the DFT bands structure, the symmetry-protected gapless points at Γ and A are double Weyl points with chirality ±2. (See Sec. II B in Ref. [48] for details.) However, the band splitting along Γ-A is very small (maximum splitting about 2 meV), and thus in our simplified NN-hopping model, we neglect the band splitting along Γ-A for simplicity. Although such simplification in our model will make the two double Weyl points merge into an accidental nodal line along Γ-A, it will be convenient for future study on the correlated physics, since it makes the eigenvectors of the Hamiltonian independent of k_z.

Both Refs. [9,16] contain two-band PM models constructed from d_{xz} and d_{yz} on Cu. However, the two-band PM model in Ref. [16] has mirror symmetry along y, which we do not include in our model since the DFT calculation indicates a considerable breaking of the mirror symmetry. The two-band PM models in both Refs. [9,16] have considerably different parameter values than ours. Reference [9] shows double Weyl points at Γ and A in their two-band model, for which they choose to include the small band splitting along Γ-A in their model.

V. INTERACTING HAMILTONIAN

We use the constraint random phase approximation (cRPA) method [88–91] to compute the screened Coulomb interaction for the (d_{xz}, d_{yz}) orbitals of Cu near E_f for two Cu-doped structure of $Pb_9Cu_1(PO_4)_6O$ and $Pb_9Cu_1(PO_4)_6(OH)_2$. In Table III, we list the values of Hubbard-Kanamori parameters, i.e., the onsite intra-orbital Hubbard $\mathcal{U}$, inter-orbital $\mathcal{U}'$, and onsite exchange $\mathcal{J}$. The interacting Hamiltonian can be

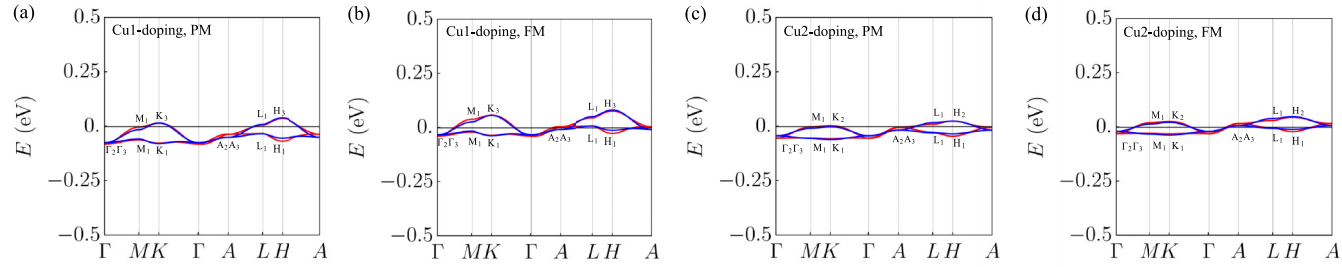

FIG. 11. Comparison of the relaxed DFT (red) and two-band tight-binding model band structures (blue) and irreps for $Pb_9Cu(PO_4)_6(OH)_2$ in the specified Cu doping and magnetic properties. The relaxed DFT and the NN-hopping tight-binding model (blue) are in close agreement. The expression of the model and the values of the model parameters are specified in Sec. II in Ref. [48]. Note that this is a two-band model, so the quantum geometric tensor of both bands, taken together, vanishes.

constructed as

$$\hat{H}_{\text{int}} = \mathcal{U}\sum_{im} n_{im\uparrow}n_{im\downarrow} + \mathcal{U}'\sum_{i,m\neq m'} n_{im\uparrow}n_{im'\downarrow} + (\mathcal{U}'-\mathcal{J})\sum_{i,m<m',\sigma} n_{im\sigma}n_{im'\sigma} + \mathcal{J}\sum_{i,m\neq m'}(-c^{\dagger}_{im\uparrow}c_{im\downarrow}c^{\dagger}_{im'\downarrow}c_{im'\uparrow} + c^{\dagger}_{im\uparrow}c^{\dagger}_{im\downarrow}c_{im'\downarrow}c_{im'\uparrow}), \tag{4}$$

where i is the site index and m the orbital index. We remark that the *ab initio* Hubbard-Kanamori parameters may need to be renormalized as the two quasiflat bands near E_f also have weights of other orbitals.

Comments on flat bands and interactions

Flat bands are thought to be beneficial for strongly correlated phases since the interaction strength necessarily dominates over the single-particle bandwidth. However, the quantum geometry of the flat bands is another essential ingredient in determining the nature of the resulting strongly correlated phases.

For instance, in the single-band square lattice Hubbard model at half filling, the flat band limit $t \to 0$ yields a fully decoupled lattice (the atomic limit) which is a perfect paramagnet. It is $O(t^2/U)$ corrections that stabilize an antiferromagnetic phase. If, however, the interaction strength is much larger than a set of isolated bands but smaller than the gap between these bands and their complement, a different set of phases can emerge. In the repulsive case, ferromagnetism can be proven [43,44], and superconductivity (or phase separation) for attractive case [26,34,43]. Features of the many-body phase, for instance the mass of the Cooper pair, stiffness of the spin wave, and a lower bound on the electron-phonon coupling are determined by quantum geometry [26,34,92].

To entertain the possibility of superconductivity in flat bands, we recall that the mean-field critical temperature in flat bands will be proportional to the interaction strength [22]. Although this scenario is exponentially improved over one-band BCS theory, it still requires an attractive interaction of roughly 100 meV. This order of magnitude is larger than the bandwidth of the two-band model in the OH structure, and roughly equal to the bandwidth of the upper Cu bands in the four-band model for the O structure. (We note in this case that the band gap is small, and projecting the interaction to the flat bands may not be justified.) The repulsive Coulomb interaction we computed is eV scale, and is much larger than the total bandwidth of both tight-binding models.

Two recent papers [9,20] have proposed models where one of the Cu bands is perfectly flat. Although the two Cu bands together form an indecomposable elementary band representation with trivial topology, analyzing only one of the two bands (per spin) away from their degeneracy points at Γ and A can show strong quantum geometry. It is only appropriate to consider strong coupling groundstate a single flat (gapless) band in the limit where the interaction strength is much smaller than the bandwidth. This limit, while interesting and worthy of study, places an upper bound on the interaction strength which limits its applicability to a high-temperature phase.

TABLE III. The *ab-initio* Hubbard-Kanamori parameters. In the table, $\mathcal{U}, \mathcal{U}', \mathcal{J}$ denotes the onsite intraorbital Hubbard, interorbital Hubbard, and onsite exchange interaction. All numbers are in eV.

Phase	$\mathcal{U}$	$\mathcal{U}'$	$\mathcal{J}$
$Pb_9Cu_1(PO_4)_6O$ Cu1	2.75	1.71	0.52
$Pb_9Cu_1(PO_4)_6O$ Cu2	3.53	2.38	0.58
$Pb_9Cu_1(PO_4)_6(OH)_2$ Cu1	2.88	1.99	0.45
$Pb_9Cu_1(PO_4)_6(OH)_2$ Cu2	1.85	0.96	0.14

VI. FURTHER VERIFICATION AND TESTS

A. Immediate experiments

As we experimentally found that samples are multiphase, short-term experiments should focus on isolating the different phases and characterizing their compositions and structures. Also several more synthesis should be performed to confirm that the outcomes are repeatable. Once we know reliably the outcome of the synthesis the sample needs to be thoroughly characterized with a wide range of methods. SEM/EDX will be a good first attempt to analyze how many different phases are in the materials and what their respective compositions are. It would be ideal if those phases can be separated either manually of in different synthesis attempts targeting the

respective compositions found via SEM/EDX. As we showed it is possible to pick single crystals from at least one phase.

B. Chemical structure verification

Once phase-pure materials are obtained, they can be thoroughly characterized. If single crystals are obtained, SXRD is ideal in combination with chemical analysis such as SEM/EDX or, if enough samples can be separated, ICP-OES. Otherwise PXRD in combination with Rietveld refinement will be necessary. If the phases are not crystalline, the structural characterization becomes more complicated and chemical analysis is a more important first step, likely to be followed by high-resolution electron microscopy.

Characterization of physical properties is most meaningful on single-phase materials and can be performed after through characterization of all components of the samples. Similarly, theoretical analysis of the electronic structures is most meaningful if the final crystal structures are known.

C. Theoretical analysis

Once the chemical structure is firmly established and the set of bands at the Fermi level is settled, the bands must be fully analyzed based on the principles outlined in this paper, including orbital, quantum geometric, topological, and localization content in all the multiple phases that result from the reaction. The interacting Hamiltonian must then be derived and with it the values of the Hubbard U. Then the ground state of the system must be determined. Even if not superconducting, one must still explain the levitation properties shown in initial experiments—either large diamagnetism or some flavor of ferromagnetism. The phonons, and more importantly the electron-phonon interaction need to be obtained; an understanding is needed of the rather flat Pb phonon bands on the $k_z = \pi$ plane that seem to become negative at low temperature. If indeed, however, the sample does turn out to be superconducting, short of being a fundamental discovery, it would also point out the limitation of our theoretical understanding of the mechanisms that create it.

VII. CONCLUSIONS

Assuming the reported structure and the location of the Cu dopants, we have performed first principle calculations of the electronic structure of $Pb_9Cu_1(PO_4)_6O$ and $Pb_9Cu_1(PO_4)_6(OH)_2$. We find that the bands are almost flat, localized on the Cu atoms, and have weak quantum geometry and trivial topology. Hence in a "flat-band superconductivity" scenario, already alluded to previously, our calculation of the quantum geometric properties of the active bands shows that such a phase would have extremely small superfluid stiffness even at zero temperature. Instead, their flatness and the strong Coulomb repulsion are compatible with the (anti/)ferromagnetic ground states found in calculations. The phonon spectra seem to contain imaginary phonons for both high and low-temperature paramagnetic phases (with the reported unrelaxed structure). The experimental findings also do not, as of yet, strongly suggest the presence of superconductivity. Hence either the reported structure is incorrect, or the *ab initio* calculations and the structure are correct but then further give rise to a nonsuperconducting ground state, or the *ab initio* calculations are incorrect due to large correlation, or the simplified treatment for disordered structures might not faithfully represent the complexity, thus warranting the exploration of more advanced computational algorithms. In fact, our preliminary experiments and structural solutions point to LK-99 being a multiphase material, where the part that structurally agrees with a doped version of Pb apatite is transparent and thus probably not superconducting. Either way, this points to the difficulty of predicting and/or explaining superconductors by *ab initio* methods, even when they exist. It also suggests that extra cases be taken in the literature, both experimental and theoretical. Experimentally, samples need to be much more carefully analyzed with a wide range of diffraction and spectroscopic methods. The individual phases should be isolated and their properties should be studied separately. Theoretically, one must at the very minimum check the correct symmetry of the states, their localization and topology, and try to obtain superconductivity from the first principle Hamiltonian, rather than introducing it by hand in a BdG formalism. These represent hard challenges that only serious investigations can overcome.

ACKNOWLEDGMENTS

H.H. and Y.J. were supported by the European Research Council (ERC) under the European Unions Horizon 2020 research and innovation program (Grant Agreement No. 101020833). D.C. acknowledges the hospitality of the Donostia International Physics Center, at which this work was carried out. J.H-A. is supported by a Hertz Fellowship. D.C. and B.A.B. were supported by the Simons Investigator Grant No. 404513, the Gordon and Betty Moore Foundation through Grant No. GBMF8685 towards the Princeton theory program, the Gordon and Betty Moore Foundations EPiQS Initiative (Grant No. GBMF11070), Office of Naval Research (ONR Grant No. N00014-20-1-2303), BSF Israel US foundation No. 2018226, NSF-MERSEC (Grant No. MERSEC DMR 2011750). J.Y. is supported by the Gordon and Betty Moore Foundation through Grant No. GBMF8685 towards the Princeton theory program. B.A.B. and C.F. are also part of the SuperC collaboration. Y.J. and S.B-C. acknowledge financial support from the MINECO of Spain through the project PID2021- 122609NB-C21 and by MCIN and by the European Union Next Generation EU/PRTR-C17.I1, as well as by IKUR Strategy under the collaboration agreement between Ikerbasque Foundation and DIPC on behalf of the Department of Education of the Basque Government. BAB also acknowledges support the European Research Council (ERC) under the European Unions Horizon 2020 research and innovation program (Grant Agreement No. 101020833). J.H. and D.C. are supported by DOE Grant No. DE-SC0016239. J.H is also supported by a Hertz Fellowship. C.H.H, P.S.B, and E.L.G are supported by DMR-1956403, and the Research Corporation for Science Advancement (Cottrell Scholar Program) for nontenured faculty. We are grateful to T. T. Debela, A. Walsh, D. Scanlon, A. Rosen, and C. Musgrave for helpful discussions related to defect formation enthalpy calculations. The authors acknowledge the use of Princeton Imaging and Analysis Center, which is partially supported by the Princeton

Center for Complex Materials, a National Science Foundation (NSF) MRSEC program (DMR-2011750). The authors would also like to acknowledge G. Cheng for helping with carbon coating. L.M.S. is supported by the Gordon and Betty Moore Foundations EPIQS initiative through Grant No. GBMF9064, as well as the David and Lucille Packard foundation. SBL is supported by the National Science Foundation Graduate Research Fellowship Program under Grant No. (DGE-2039656). Any opinions, findings, and conclusions or recommendations expressed in this material are those of the author(s) and do not necessarily reflect the views of the National Science Foundation.

S.B.L. grew crystals and solved the SCXD solutions reported in this paper.

[1] S. Lee, J.-H. Kim, and Y.-W. Kwon, The first room-temperature ambient-pressure superconductor, arXiv:2307.12008 [cond-mat].

[2] S. Lee, J. Kim, H.-T. Kim, S. Im, S. An, and K. H. Auh, Superconductor Pb_{10-x} $Cu_x(PO_4)_6$ O showing levitation at room temperature and atmospheric pressure and mechanism, arXiv:2307.12037 [cond-mat]

[3] P. Abramian, A. Kuzanyan, V. Nikoghosyan, S. Teknowijoyo, and A. Gulian, Some remarks on possible superconductivity of composition Pb_9 CuP_6 O_{25}, arXiv:2308.01723 [cond-mat].

[4] G. Baskaran, Broad band mott localization is all you need for hot superconductivity: Atom Mott insulator theory for Cu-Pb apatite, arXiv:2308.01307 [cond-mat].

[5] S. Brückner, G. Lusvardi, L. Menabue, and M. Saladini, Crystal structure of lead hydroxyapatite from powder X-ray diffraction data, Inorg. Chim. Acta **236**, 209 (1995).

[6] J. Cabezas-Escares, N. F. Barrera, C. Cardenas, and F. Munoz, Theoretical insight on the LK-99 material, arXiv:2308.01135 [cond-mat].

[7] S. M. Griffin, Origin of correlated isolated flat bands in copper-substituted lead phosphate apatite, arXiv:2307.16892 [cond-mat].

[8] K. Guo, Y. Li, and S. Jia, Ferromagnetic half levitation of LK-99-like synthetic samples, arXiv:2308.03110 [cond-mat].

[9] M. M. Hirschmann and J. Mitscherling, Tight-binding models for SG 143 (P3) and application to recent DFT results on copper-doped lead apatite, arXiv:2308.03751 [cond-mat].

[10] Q. Hou, W. Wei, X. Zhou, Y. Sun, and Z. Shi, Observation of zero resistance above 100° K in Pb_{10-x} $Cu_x(PO_4)_6$ O, arXiv:2308.01192 [cond-mat].

[11] K. Kumar, N. K. Karn, and V. P. S. Awana, Synthesis of possible room temperature superconductor LK-99:Pb_9 $Cu(PO_4)_6$ O, arXiv:2307.16402 [cond-mat].

[12] K. Kumar, N. K. Karn, Y. Kumar, and V. P. S. Awana, Absence of superconductivity in LK-99 at ambient conditions, arXiv:2308.03544 [cond-mat].

[13] R. Kurleto, S. Lany, D. Pashov, S. Acharya, M. van Schilfgaarde, and D. S. Dessau, Pb-apatite framework as a generator of novel flat-band CuO based physics, including possible room temperature superconductivity, arXiv:2308.00698 [cond-mat].

[14] J. Lai, J. Li, P. Liu, Y. Sun, and X.-Q. Chen, First-principles study on the electronic structure of Pb_{10-x} $Cu_x(PO_4)_6$ O (x=0, 1), arXiv:2307.16040 [cond-mat].

[15] L. Liu, Z. Meng, X. Wang, H. Chen, Z. Duan, X. Zhou, H. Yan, P. Qin, and Z. Liu, Semiconducting transport in Pb_{10-x} $Cu_x(PO_4)_6$ O sintered from Pb_2 SO_5 and Cu_3 P, arXiv:2307.16802 [cond-mat, physics:physics].

[16] H. Oh and Y.-H. Zhang, S-wave pairing in a two-orbital t-J model on triangular lattice: Possible application to Pb_{10-x} $Cu_x(PO_4)_6$ O, arXiv:2308.02469 [cond-mat].

[17] L. Si and K. Held, Electronic structure of the putative room-temperature superconductor Pb_9 $Cu(PO_4)_6$ O, Phys. Rev. B **108**, L121110 (2023).

[18] Y. Sun, K.-M. Ho, and V. Antropov, Metallization and spin fluctuations in Cu-doped lead apatite, Phys. Rev. Mater. **7**, 114804 (2023).

[19] K. Tao, R. Chen, L. Yang, J. Gao, D. Xue, and C. Jia, The Cu induced ultraflat band in the room-temperature superconductor Pb_{10-x} $Cu_x(PO_4)_6$ O_4 ($x = 0, 0.5$), arXiv:2308.03218 [cond-mat].

[20] O. Tavakol and T. Scaffidi, Minimal model for the flat bands in copper-substituted lead phosphate apatite, arXiv:2308.01315 [cond-mat].

[21] H. Wu, L. Yang, B. Xiao, and H. Chang, Successful growth and room temperature ambient-pressure magnetic levitation of LK-99, arXiv:2308.01516 [cond-mat].

[22] S. Peotta and P. Törmä, Superfluidity in topologically nontrivial flat bands, Nat. Commun. **6**, 8944 (2015).

[23] P. Törmä, S. Peotta, and B. A. Bernevig, Superconductivity, superfluidity and quantum geometry in twisted multilayer systems, Nat. Rev. Phys. **4**, 528 (2022).

[24] X. Zhou, W.-S. Lee, M. Imada, N. Trivedi, P. Phillips, H.-Y. Kee, P. Törmä, and M. Eremets, High-temperature superconductivity, Nat. Rev. Phys. **3**, 462 (2021).

[25] M. Tovmasyan, S. Peotta, L. Liang, P. Törmä, and S. D. Huber, Preformed pairs in flat Bloch bands, Phys. Rev. B **98**, 134513 (2018).

[26] M. Tovmasyan, S. Peotta, P. Törmä, and S. D. Huber, Effective theory and emergent SU(2) symmetry in the flat bands of attractive Hubbard models, Phys. Rev. B **94**, 245149 (2016).

[27] L. Liang, T. I. Vanhala, S. Peotta, T. Siro, A. Harju, and P. Törmä, Band geometry, Berry curvature, and superfluid weight, Phys. Rev. B **95**, 024515 (2017).

[28] K.-E. Huhtinen, J. Herzog-Arbeitman, A. Chew, B. A. Bernevig, and P. Törmä, Revisiting flat band superconductivity: Dependence on minimal quantum metric and band touchings, Phys. Rev. B **106**, 014518 (2022).

[29] X. Hu, T. Hyart, D. I. Pikulin, and E. Rossi, Geometric and conventional contribution to the superfluid weight in twisted bilayer graphene, Phys. Rev. Lett. **123**, 237002 (2019).

[30] G. Jiang and Y. Barlas, Pair density waves from local band geometry, Phys. Rev. Lett. **131**, 016002 (2023).

[31] D. Mao and D. Chowdhury, Diamagnetic response and phase stiffness for interacting isolated narrow bands, Proc. Natl. Acad. Sci. **120**, e2217816120 (2023).

[32] J. S. Hofmann, E. Berg, and D. Chowdhury, Superconductivity, charge density wave, and supersolidity in flat bands with a tunable quantum metric, Phys. Rev. Lett. **130**, 226001 (2023).

[33] P. Törmä, L. Liang, and S. Peotta, Quantum metric and effective mass of a two-body bound state in a flat band, Phys. Rev. B **98**, 220511(R) (2018).

[34] J. Herzog-Arbeitman, A. Chew, K.-E. Huhtinen, P. Törmä, and B. A. Bernevig, Many-body superconductivity in topological flat bands, arXiv:2209.00007 [cond-mat.str-el].

[35] J. Yu, Y.-A. Chen, and S. Das Sarma, Euler-obstructed Cooper pairing: Nodal superconductivity and hinge Majorana zero modes, Phys. Rev. B **105**, 104515 (2022).

[36] J. Yu, M. Xie, F. Wu, and S. Das Sarma, Euler-obstructed nematic nodal superconductivity in twisted bilayer graphene, Phys. Rev. B **107**, L201106 (2023).

[37] F. Xie, Z. Song, B. Lian, and B. A. Bernevig, Topology-bounded superfluid weight in twisted bilayer graphene, Phys. Rev. Lett. **124**, 167002 (2020).

[38] J. Herzog-Arbeitman, V. Peri, F. Schindler, S. D. Huber, and B. A. Bernevig, Superfluid weight bounds from symmetry and quantum geometry in flat bands, Phys. Rev. Lett. **128**, 087002 (2022).

[39] D. Călugăru, A. Chew, L. Elcoro, Y. Xu, N. Regnault, Z.-D. Song, and B. A. Bernevig, General construction and topological classification of crystalline flat bands, Nat. Phys. **18**, 185 (2022).

[40] Y. Hwang, J.-W. Rhim, and B.-J. Yang, Flat bands with band crossings enforced by symmetry representation, Phys. Rev. B **104**, L081104 (2021).

[41] Y. Hwang, J.-W. Rhim, and B.-J. Yang, General construction of flat bands with and without band crossings based on wave function singularity, Phys. Rev. B **104**, 085144 (2021).

[42] R. Resta, The insulating state of matter: A geometrical theory, Eur. Phys. J. B **79**, 121 (2011).

[43] E. H. Lieb, Two theorems on the Hubbard model, Phys. Rev. Lett. **62**, 1201 (1989).

[44] A. Mielke and H. Tasaki, Ferromagnetism in the Hubbard model, Commun. Math. Phys. **158**, 341 (1993).

[45] S. V. Krivovichev and P. C. Burns, Crystal chemistry of lead oxide phosphates: crystal structures of $Pb_4O(PO_4)_2$, $Pb_8O_5(PO_4)_2$ and $Pb_{10}(PO_4)_6O$, Z. Kristallogr. - Cryst. Mater. **218**, 357 (2003).

[46] B. Bradlyn, L. Elcoro, J. Cano, M. G. Vergniory, Z. Wang, C. Felser, M. I. Aroyo, and B. A. Bernevig, Topological quantum chemistry, Nature (London) **547**, 298 (2017).

[47] L. Elcoro, B. J. Wieder, Z. Song, Y. Xu, B. Bradlyn, and B. A. Bernevig, Magnetic topological quantum chemistry, Nat. Commun. **12**, 5965 (2021).

[48] See Supplemental Material at http://link.aps.org/supplemental/10.1103/PhysRevB.108.235127 for additional calculations, figures, and details of the models.

[49] S. Zhu, W. Wu, Z. Li, and J. Luo, First order transition in $Pb_{10-x}Cu_x(PO_4)6O(0.9 < x < 1.1)$ containing Cu_2S, arXiv:2308.04353 [cond-mat.supr-con].

[50] M. Tinkham, *Introduction to Superconductivity*, 2nd ed. (Dover Publications, 2004).

[51] F. Yu, M. Hirschberger, T. Loew, G. Li, B. J. Lawson, T. Asaba, J. B. Kemper, T. Liang, J. Porras, G. S. Boebinger, J. Singleton, B. Keimer, L. Li, and N. P. Ong, Magnetic phase diagram of underdoped $YBa_2Cu_3O_y$ inferred from torque magnetization and thermal conductivity, Proc. Natl. Acad. Sci. **113**, 12667 (2016).

[52] C. Freysoldt, B. Grabowski, T. Hickel, J. Neugebauer, G. Kresse, A. Janotti, and C. G. Van de Walle, First-principles calculations for point defects in solids, Rev. Mod. Phys. **86**, 253 (2014).

[53] G. Kresse and J. Furthmüller, Efficiency of ab-initio total energy calculations for metals and semiconductors using a plane-wave basis set, Comput. Mater. Sci. **6**, 15 (1996).

[54] G. Kresse and J. Hafner, Ab initio molecular dynamics for open-shell transition metals, Phys. Rev. B **48**, 13115 (1993).

[55] G. Kresse and J. Hafner, *Ab initio* molecular dynamics for liquid metals, Phys. Rev. B **47**, 558 (1993).

[56] G. Kresse and J. Hafner, *Ab initio* molecular-dynamics simulation of the liquid-metalamorphous-semiconductor transition in germanium, Phys. Rev. B **49**, 14251 (1994).

[57] G. Kresse and J. Furthmüller, Efficient iterative schemes for *ab initio* total-energy calculations using a plane-wave basis set, Phys. Rev. B **54**, 11169 (1996).

[58] J. P. Perdew, K. Burke, and M. Ernzerhof, Generalized gradient approximation made simple, Phys. Rev. Lett. **77**, 3865 (1996).

[59] N. Marzari and D. Vanderbilt, Maximally localized generalized Wannier functions for composite energy bands, Phys. Rev. B **56**, 12847 (1997).

[60] I. Souza, N. Marzari, and D. Vanderbilt, Maximally localized Wannier functions for entangled energy bands, Phys. Rev. B **65**, 035109 (2001).

[61] N. Marzari, A. A. Mostofi, J. R. Yates, I. Souza, and D. Vanderbilt, Maximally localized Wannier functions: Theory and applications, Rev. Mod. Phys. **84**, 1419 (2012).

[62] G. Pizzi, V. Vitale, R. Arita, S. Blügel, F. Freimuth, G. Géranton, M. Gibertini, D. Gresch, C. Johnson, T. Koretsune *et al.*, Wannier90 as a community code: new features and applications, J. Phys.: Condens. Matter **32**, 165902 (2020).

[63] A. Togo, F. Oba, and I. Tanaka, First-principles calculations of the ferroelastic transition between rutile-type and $CaCl_2$-type SiO_2 at high pressures, Phys. Rev. B **78**, 134106 (2008).

[64] C.-J. Liao, F.-H. Lin, K.-S. Chen, and J.-S. Sun, Thermal decomposition and reconstitution of hydroxyapatite in air atmosphere, Biomaterials **20**, 1807 (1999).

[65] T. Negas and R. Roth, High temperature dehydroxylation of apatitic phosphates, J. Res. Natl. Bur. Stand., Sect. A **72A**, 783 (1968).

[66] R. M. H. Verbeeck, H. J. M. Heiligers, F. C. M. Driessens, and H. G. Schaeken, Effect of dehydration of calcium hydroxylapatite on its cell parameters, Z. Anorg. Allg. Chem. **466**, 76 (1980).

[67] A. Walsh, Correcting the corrections for charged defects in crystals, npj Comput. Mater. **7**, 72 (2021).

[68] C. Freysoldt, J. Neugebauer, and C. G. Van de Walle, Fully *ab initio* finite-size corrections for charged-defect supercell calculations, Phys. Rev. Lett. **102**, 016402 (2009).

[69] H. Bian, T. Liu, D. Li, Z. Xu, J. Lian, M. Chen, J. Yan, and S. F. Liu, Unveiling the effect of interstitial dopants on CO_2 activation over $CsPbBr_3$ catalyst for efficient photothermal CO_2 reduction, Chem. Eng. J. **435**, 135071 (2022).

[70] R. Černý, K. Yvon, M. Wakihara, and P. Fischer, Location of oxygen in the structure of the Chevrel phase $Cu_{1.8}Mo_6S_{8-x}O_x$, J. Alloys Compd. **209**, L29 (1994).

[71] S. Zhu, W. Wu, Z. Li, and J. Luo, First order transition in $Pb_{10-x}Cu_x(PO_4)_6o$ $(0.9 < x < 1.1)$ containing Cu_2s, arXiv:2308.04353 [cond-mat.supr-con].

[72] P. K. Jain, Phase transition of copper(I) sulfide and its implication for purported superconductivity of LK-99, J. Phys. Chem. C **127**, 18253 (2023).

[73] B. A. Inc., Apex2 (2012), accessed August 7, 2023.

[74] V. Petricek, L. Palatinus, J. Plasil, and M. Dusek, Jana2020 a new version of the crystallographic computing system Jana, Z. Kristallogr. Cryst. Mater. **238**, 271 (2023).

[75] L. Palatinus and G. Chapuis, SUPERFLIP–a computer program for the solution of crystal structures by charge flipping in arbitrary dimensions, J. Appl. Crystallogr. **40**, 786 (2007).

[76] K. Momma and F. Izumi, Vesta: A three-dimensional visualization system for electronic and structural analysis, J. Appl. Cryst. **41**, 653 (2008).

[77] $Pb_{10}(PO_4)_6O(Pb_{10}[PO_4]_6O)$ crystal structure: Datasheet from "pauling file multinaries edition–2022" in springermaterials, https://materials.springer.com/isp/crystallographic/docs/sd_1616772 (Springer-Verlag Berlin Heidelberg & Material Phases Data System (MPDS), Switzerland & National Institute for Materials Science (NIMS), Japan, 2023).

[78] $Pb_{10}(PO4)_6(OH)_2(Pb_5[PO_4]_3[OH])$ crystal structure: Datasheet from "pauling file multinaries edition–2022" in springermaterials, https://materials.springer.com/isp/crystallographic/docs/sd_1003884 (Springer-Verlag Berlin Heidelberg & Material Phases Data System (MPDS), Switzerland & National Institute for Materials Science (NIMS), Japan, 2023).

[79] $Pb_{10}(PO4)_6(OH)_2(Pb_5[PO_4]_3[OH])$ crystal structure: Datasheet from "pauling file multinaries edition–2022" in springermaterials, https://materials.springer.com/isp/crystallographic/docs/sd_1714473 (Springer-Verlag Berlin Heidelberg & Material Phases Data System (MPDS), Switzerland & National Institute for Materials Science (NIMS), Japan, 2023).

[80] K. Zhu, K. Yanagisawa, R. Shimanouchi, A. Onda, K. Kajiyoshi, and J. Qiu, Hydrothermal synthesis and crystallographic Study of Sr-Pb hydroxyapatite solid solutions, J. Ceram. Soc. Jpn. **115**, 873 (2007).

[81] Pb10(po4)6(oh)2 (pb5[po4]3[oh]) crystal structure: Datasheet from "pauling file multinaries edition–2022" in springermaterials, https://materials.springer.com/isp/crystallographic/docs/sd_1631620 (Springer-Verlag Berlin Heidelberg & Material Phases Data System (MPDS), Switzerland & National Institute for Materials Science (NIMS), Japan, 2023).

[82] K. Zhu, J. Qiu, H. Ji, K. Yanagisawa, R. Shimanouchi, A. Onda, and K. Kajiyoshi, Crystallographic study of lead-substituted hydroxyapatite synthesized by high-temperature mixing method under hydrothermal conditions, Inorg. Chim. Acta **363**, 1785 (2010).

[83] J. Y. Kim, B. A. Hunter, R. R. Fenton, and B. J. Kennedy, Neutron powder diffraction study of lead hydroxyapatite, Australian J. Chem. **50**, 1061 (1997).

[84] A. Zunger, S.-H. Wei, L. Ferreira, and J. E. Bernard, Special quasirandom structures, Phys. Rev. Lett. **65**, 353 (1990).

[85] L. Monacelli, R. Bianco, M. Cherubini, M. Calandra, I. Errea, and F. Mauri, The stochastic self-consistent harmonic approximation: calculating vibrational properties of materials with full quantum and anharmonic effects, J. Phys.: Condens. Matter **33**, 363001 (2021).

[86] O. Hellman, P. Steneteg, I. A. Abrikosov, and S. I. Simak, Temperature dependent effective potential method for accurate free energy calculations of solids, Phys. Rev. B **87**, 104111 (2013).

[87] X.-G. Zhao, G. M. Dalpian, Z. Wang, and A. Zunger, Polymorphous nature of cubic halide perovskites, Phys. Rev. B **101**, 155137 (2020).

[88] F. Aryasetiawan, M. Imada, A. Georges, G. Kotliar, S. Biermann, and A. Lichtenstein, Frequency-dependent local interactions and low-energy effective models from electronic structure calculations, Phys. Rev. B **70**, 195104 (2004).

[89] I. Solovyev and M. Imada, Screening of Coulomb interactions in transition metals, Phys. Rev. B **71**, 045103 (2005).

[90] F. Aryasetiawan, K. Karlsson, O. Jepsen, and U. Schönberger, Calculations of Hubbard $\boldsymbol{U}$ from first-principles, Phys. Rev. B **74**, 125106 (2006).

[91] T. Miyake, F. Aryasetiawan, and M. Imada, *Ab initio* procedure for constructing effective models of correlated materials with entangled band structure, Phys. Rev. B **80**, 155134 (2009).

[92] J. Yu, C. J. Ciccarino, R. Bianco, I. Errea, P. Narang, and B. A. Bernevig, Nontrivial quantum geometry and the strength of electron-phonon coupling, arXiv:2305.02340 [cond-mat.supr-con].